PHYSICAL REVIEW FLUIDS **8**, 044703 (2023)

Experimental investigation of vortex-induced vibrations of a flexibly mounted cylinder in a shear-thinning fluid

Pieter R. Boersma, Jonathan P. Rothstein, and Yahya Modarres-Sadeghi*
Department of Mechanical and Industrial Engineering, University of Massachusetts, Amherst, Massachusetts 01003, USA

(Received 20 July 2022; accepted 3 April 2023; published 24 April 2023)

A flexibly mounted cylinder placed in a Newtonian flow undergoes vortex-induced induced vibrations (VIV) during which the shedding frequency and the oscillation frequency are synchronized. In Newtonian fluids, VIV occurs at Reynolds numbers as low as Re = 19. Here, we show that the expected VIV response of the cylinder can be greatly affected if the viscosity of the fluid is shear thinning, by conducting VIV experiments in a series of fluids of xanthan gum solutions of increasing concentration and increasing shear-thinning intensity. While the VIV response of the weakly shear-thinning fluid closely resembles the VIV response of Newtonian fluids, we show that by increasing concentration and shear thinning, the critical Reynolds number at which VIV occurs increases, while the reduced velocity at which lock-in begins, the width of the lock-in range, and the oscillation amplitude decrease. Beyond a critical concentration, VIV is completely suppressed over the entire range of Reynolds numbers studied here. The increase in critical Reynolds number and the reduction in the width of the lock-in range and the amplitude are likely caused by the increased viscosity and increased momentum diffusion of the shed vortices in the cylinder's wake, where the shear rate is small and the viscosity is large as it has recovered back toward its zero-shear-rate limit. The reduction in the critical reduced velocity is caused by an increase in the vortex shedding frequency as the fluid becomes more shear thinning. For the most shear-thinning fluid tested where VIV is completely suppressed, the vortices are shed very far from the cylinder and do not cause any oscillations.

DOI: 10.1103/PhysRevFluids.8.044703

I. INTRODUCTION

When a bluff body is placed in Newtonian flow, vortices are shed in its wake. The frequency of this vortex shedding increases linearly with increasing flow velocity following the Strouhal law. If the bluff body (e.g., a cylinder) is flexibly mounted, at a certain flow velocity the shedding frequency equals the natural frequency of the system and the body starts to oscillate. Theses oscillations then result in a deviation of the shedding frequency from the linear increase predicted by the Strouhal law, and for a range of reduced velocities (defined as $U^* = U/Df_n$, where U is the free stream velocity, D is the cylinder diameter, and f_n is the structure's natural frequency), the shedding frequency and the oscillation frequency become synchronized. This range is called the lock-in range and the observed oscillations are called vortex-induced vibrations (VIV) [1–4].

VIV is a canonical problem in fluid-structure interactions (FSI) and has been studied extensively for both flexibly mounted and flexible structures. For a flexibly mounted structure placed in flow, VIV studies have considered cases of a one-degree-of-freedom (1DOF) system allowed to oscillate in the direction perpendicular to the direction of motion [cross-flow (CF) direction] [1,2], 1DOF

---

[*] modarres@engin.umass.edu

systems allowed to oscillate only in the direction of flow [inline (IL) direction] [5,6], or at any angle in between [7]. Cases of two-DOF (2DOF) systems in which the cylinder is allowed to oscillate in both the CF and IL directions have been considered as well [8–10]. Some recent studies have shown that VIV can occur also at subcritical Reynolds numbers (defined as $\mathrm{Re} = UD/\nu$, where ν is the kinematic viscosity of the fluid), i.e., Reynolds numbers smaller than the minimum for which vortex shedding is observed in the wake of a fixed cylinder: $\mathrm{Re} = 47$ [11]. Numerical and experimental results have shown that CF VIV can be observed at Reynolds numbers as low as $\mathrm{Re} = 19$ [12,13] for flexibly mounted cylinders and as low as $\mathrm{Re} = 20$ for flexible cylinders [14].

The response of a flexibly mounted cylinder to the flow of a non-Newtonian fluid is much less well explored. In a series of recent studies, the response of flexible or flexibly mounted cylinders and sheets placed in the flow of viscoelastic fluids was studied [15–20]. For viscoelastic fluids, purely elastic flow instabilities can occur at high Weissenberg numbers, $\mathrm{Wi} = \lambda\dot{\gamma} \gg 1$ (where λ is the fluid relaxation time and $\dot{\gamma}$ is the shear rate), and very small Reynolds numbers, $\mathrm{Re} \ll 1$. These elastic flow instabilities are capable of driving the motion of flexible or flexibly-mounted structures placed in flow [15–20]. Viscoelastic fluid-structure interactions (VFSI) have been studied for flexible sheets [15], flexible [16] and flexibly mounted cylinders [20], and cantilevered beams in both large-scale flows [18] and within microfluidic devices [17]. In these studies, measurements of the frequency and amplitude of structural deformation, the fluid velocity profiles, and the flow-induced birefringence (FIB) were used to quantify the motion of the structure along with the time variation of the flow field and the state of elastic stress in the fluid during the oscillations. Other VFSI work has shown how microstructures such as cilia can synchronize between each other due to the elastic effects of the fluid, generating local elastic stresses that link the structures through the fluid [19]. All these studies were performed at very small Reynolds numbers; however, fluid rheology has been shown to affect flows at high Reynolds numbers as well [21,22].

Shear thinning and fluid elasticity are known to have a significant impact on vortex shedding from a fixed rigid cylinder at high Reynolds numbers. Coelho and Pinho [21,23,24] observed the effect of shear-thinning, weakly elastic fluids on the wake of a fixed cylinder in a Reynolds number range of $50 < \mathrm{Re} < 9000$. They found that shear thinning decreases both the boundary layer thickness and the formation length of the recirculation bubble, leading to an increase in the Strouhal number, $\mathrm{St} = f_s D/U$, where f_s is the vortex shedding frequency. Fluid elasticity, on the other hand, increases the formation length and decreases the Strouhal number [25–27]. Lashgari *et al.* [28] studied the instability mechanism and first bifurcation of a fixed cylinder in a fluid with a power law viscosity through numerical simulations and linear theory. When defining the Reynolds number with a zero-shear viscosity, they found that shear thinning dramatically destabilizes the flow around the cylinder and reduces the critical Reynolds number at which vortex shedding occurs, while shear-thickening fluids produce the opposite effect. They also showed with this same Reynolds number definition that the recirculation bubble length approaches the same size at the critical Reynolds number for all fluid properties. When changing their definition of the Reynolds number to a weighted average of the local Reynolds numbers over the whole domain, they found that the critical Reynolds number remains the same regardless of fluid properties and is similar to that for Newtonian fluids, $\mathrm{Re} = 47$. They found that increasing shear thinning also intensifies the vorticity close to the cylinder.

More recently, Patel *et al.* [29] numerically studied the response of a 1DOF flexibly mounted cylinder in inelastic shear-thinning and shear-thickening power law fluids. They found that when the Reynolds number is defined based on the zero-shear-rate viscosity, shear thinning enhances oscillations and shear thickening suppresses oscillations compared with the Newtonian case. They then defined a characteristic Reynolds number, $\mathrm{Re}_{\mathrm{char}} = UD/\eta_{\mathrm{char}}$, in which the viscosity is based on a characteristic shear rate around the cylinder, $\dot{\gamma}_{\mathrm{char}} = U/D$, and showed that at a constant characteristic Reynolds number, the oscillation amplitude remains constant for both shear-thinning and shear-thickening fluids independent of the zero-shear-rate viscosity and power-law index. The vortex structure in the wake, however, was quite different. They found that in the wake of the shear-thinning case the vortices decay away more quickly because the viscosity of the fluid, and therefore the rate of momentum diffusion, in low-shear-rate regions of the flow is higher than either

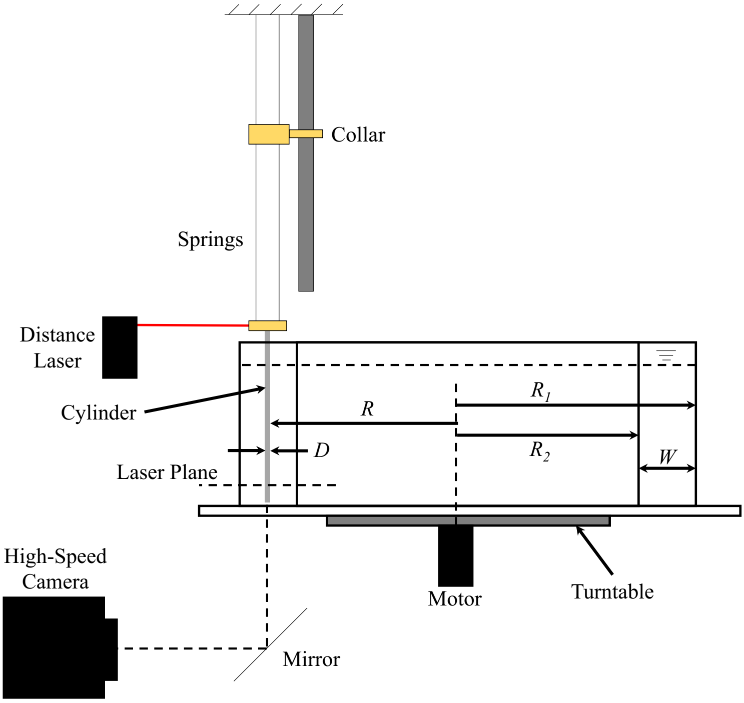

FIG. 1. A schematic of the experimental setup featuring the rotating water channel and the flexibly mounted rigid cylinder.

the Newtonian or the shear-thickening cases. Their simulations showed that, for power-law fluids, the VIV response is determined only by the local Reynolds number around the cylinder.

In the present work, we investigate experimentally the VIV response of a flexibly mounted cylinder allowed to oscillate in the CF direction in fluids that are shear thinning. We discuss how different fluid concentrations influence the VIV response of the system in various Reynolds numbers and reduced velocities. The wake is visualized through particle image velocimetry (PIV) and the influence of fluid concentration on the wake is discussed by observing local vorticity, shear rate, and extension rate.

II. EXPERIMENTAL SETUP

A circular rotating water channel (Fig. 1) was used for these experiments. The channel was comprised of two concentric acrylic cylinders with radii of $R_1 = 30$ cm and $R_2 = 25.4$ cm attached to a circular acrylic surface to produce a channel with a width of $W = 4.6$ cm and a depth of 13 cm. The channel was spun from its center and produced flow velocities in the range of 1.5–23.5 cm/s at the center of the channel at $R = 27.7$ cm. A detailed description of the setup can be found in Boersma *et al.* [13]. A 2-mm-diameter stainless steel cylinder was suspended in the center of the channel from two parallel strips of spring steel which acted as a spring. The cylinder was submerged by $53.5D$ of its length and was suspended $1.5D$ from the bottom of the channel. The channel width was $23D$. By using two strips of spring steel, the pendulum effect in the response of the cylinder was eliminated. The system's natural frequency was adjusted by increasing or decreasing the length of the springs through a vertically adjustable collar that created a clamped boundary condition. This allowed U^* to change while keeping U and the Reynolds number constant. The rectangular cross sections of the steel springs ensured that the cylinder could only oscillate in the transverse direction. The adjustable spring length resulted in a small change in mass ratio m^* (defined as the moving

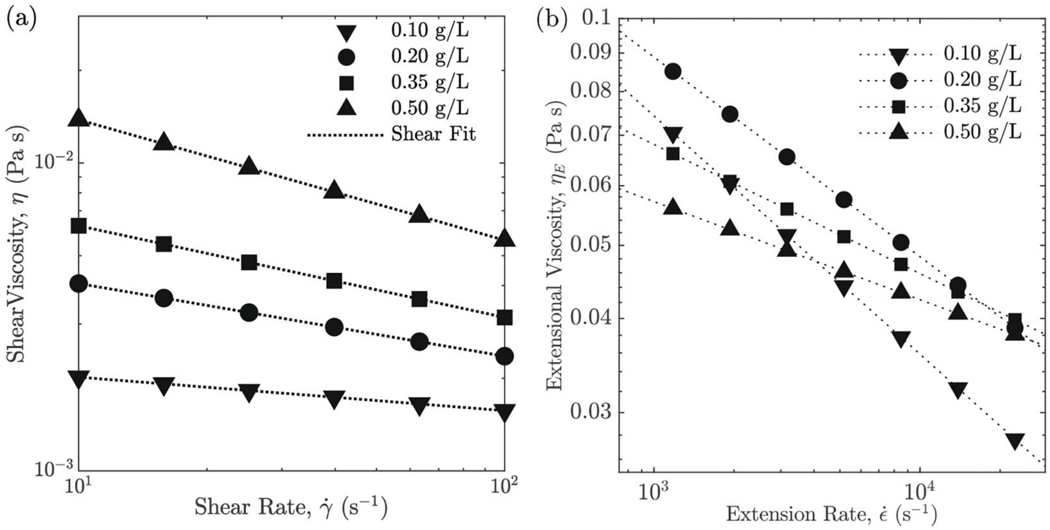

FIG. 2. (a) Shear and (b) extensional rheology measurements for various concentrations of xanthan gum in water at 20 °C. Power-law model fits are superimposed over each data set.

mass of the system divided by the displaced mass of the fluid) for each reduced velocity. We have shown previously [13] that this change in mass ratio has a negligible effect on the VIV response. The structural damping of the system was measured using a decay test in air, and was found to be on the order of 10^{-3} for all spring lengths. The rotating nature of the setup created a linearly sheared flow across the channel walls. Despite this variation in the flow velocity across the channel, since the channel width was $23D$ and the expected magnitude of the cylinder oscillations was less than $0.5D$, the flow remained relatively uniform in the range where oscillations were expected.

Cylinder oscillation amplitude and frequency were measured through a noncontacting distance-measuring laser (Panasonic HL-G11). The wake was visualized by seeding the fluids with neutrally buoyant glass spheres (Dantec Dynamics) with a diameter of 10 μm. A plane was illuminated with a laser sheet and the wake was captured using a high-speed camera (Phantom V4.2). Vorticity, shear rate, and extension rate were then calculated through PIV using an open source PIV software for MATLAB, PIVLAB v2.55 [30].

III. FLUID RHEOLOGY

The test fluids used in these experiments were created by mixing xanthan gum (Now Real Foods) in water over a concentration range of $0 \leqslant c \leqslant 0.50$ g/L. The shear viscosity of each solution was fully characterized using a Discovery HR-3 hybrid rheometer with a cone-and-plate attachment in order to determine the characteristic Reynolds number as defined by Patel *et al.* [29], $Re_{\text{char}} = UD/\eta_{\text{char}}$. The shear viscosity of each fluid is shown in Fig. 2(a). Note that only one decade of shear rate data are presented in Fig. 2(a) because over the characteristic Reynolds number range accessible in our flow cell, the shear rate varied only in the range of $10\ \text{s}^{-1} < \dot{\gamma}_{\text{char}} = U/D < 100\ \text{s}^{-1}$. At these concentrations, all the solutions were found to be shear thinning. In each case, a power law was used to satisfactorily model the fluid viscosity such that $\eta = m\dot{\gamma}^{n-1}$ [31], where η is the shear-rate-dependent viscosity and $\dot{\gamma}$ is the shear rate imposed by the rheometer. The consistency index m and the power-law exponent n for various concentrations are given in Table I, and the power-law fit is superimposed over the data in Fig. 2(a). Shear rheology was measured three times for each temperature and concentration. The resulting average power-law fits were highly repeatable and had a standard deviation of around 1% for both m and n. Increasing the xanthan gum

TABLE I. Power-law model fits to the shear viscosity of various concentrations of xanthan gum in water. The data include the consistency index (m) and the power-law exponent (n).

	m (Pa s^n)			
Concentration (g/L)	20 °C	25 °C	30 °C	n
0.10	2.9×10^{-3}	2.6×10^{-3}	2.3×10^{-3}	0.9
0.20	6.6×10^{-3}	5.6×10^{-3}	5.3×10^{-3}	0.8
0.35	1.4×10^{-2}	1.2×10^{-2}	1.1×10^{-2}	0.7
0.50	3.8×10^{-2}	3.4×10^{-2}	3.0×10^{-2}	0.6

concentration increases the power-law exponent, resulting in an increased shear-thinning effect with increasing concentration. Shear rheology measurements were performed at temperatures of 20 °C, 25 °C, and 30 °C because the fluid temperature in the experiments was not controlled but fluctuated with the room temperature. Time-temperature superposition was used to correct the viscosity used in the definition of the Reynolds number based on the temperature at the time of data collection. Table I and Fig. 2(a) present the rheology measurements at 25 °C. At other temperatures, the power-law indices were similar, varying by a maximum of ±2%, but the viscosity and the consistency index decreased with increasing temperature.

The extensional viscosity of each xanthan gum solution was characterized by conducting dripping-onto-substrate capillary breakup extensional rheology (CaBER-DoS) measurements [32–34]. In CaBER-DoS, a droplet of fluid is expelled from a nozzle at a relatively low flow velocity. When the drop makes contact with the substrate beneath the nozzle, it partially wets the substrate, creating a fluid filament between the nozzle tip and the substrate. Once formed, the fluid filament undergoes a surface-tension driven pinch-off that is the basis for capillary-break extensional rheology measurements. A more complete summary of our experimental method and equipment can be found in Rosello *et al.* [35]. For the fluids used here, depending on the fluid properties, the filament breakup is resisted by either fluid inertia or the extensional viscosity of the fluid. In the inertiocapillary breakup regime, the radius of the fluid filament will decay as $R_{\mathrm{mid}}/R_0 \propto (t_c - t)^{2/3}$, while for a Newtonian fluid in the viscocapillary breakup regime, the radius of the fluid filament will decay as $R_{\mathrm{mid}}/R_0 \propto (t_c - t)$, where R_0 is the initial radius, typically taken to be that of the nozzle, and t_c is the breakup time of the liquid filament [36]. For a power-law fluid, the filament decay does not follow either exponent, but depends on the extensional power-law index n_E. Doshi *et al.* [37] showed that for a power-law fluid in CaBER

$$\frac{R_{\mathrm{mid}}}{R_0} = \frac{\phi(n_E)\sigma}{m_E\, R_0}(t_c - t)^{n_E}, \tag{1}$$

where R_{mid} is the minimum radius of the filament; R_0 is the radius of the nozzle; $\phi(n)$ is a constant that is dependent on the power law index n_E and must be determined numerically [36]; σ is the fluid surface tension, which we have assumed to be equal to that of water; t_c is the time of capillary breakup; and t is the time of experiment. From this equation, it is possible to fully characterize a power-law fluid if the extensional power-law index is between the inertio-capillary and visco-capillary limits, $0.667 < n_E < 1.0$.

Each fluid was tested with CaBER-DoS three times and the consistency index and the power-law exponent were determined by fitting the diameter thinning to Eq. (1). The extensional viscosity of each solution was calculated from the power-law model fit defined by $\eta_E = m_E\, \dot{\epsilon}^{\,n_E - 1}$, where η_E is the extensional viscosity and $\dot{\epsilon}$ is the extension rate [31,36], and is presented in Fig. 2(b). The extension consistency index m_E and the extension power-law exponent n_E for each concentration are given in Table II, and the resulting power-law model fit is superimposed over the extensional viscosity data in Fig. 2(b). The thinning of the extensional viscosity is quite different from the thinning of the shear viscosity. While increasing xanthan gum concentration results in stronger shear

TABLE II. Power-law model fits to the extensional viscosity of various concentrations of xanthan gum in water. The data include the extension consistency indices (m_E) and the extensional power-law exponents (n_E).

Concentration (g/L)	m_E (Pa s^{n_E})	n_E
0.10	$6.6 \times 10^{-1} \pm 0.13$	0.68 ± 0.03
0.20	$5.5 \times 10^{-1} \pm 0.15$	0.74 ± 0.01
0.35	$2.2 \times 10^{-1} \pm 0.12$	0.83 ± 0.06
0.50	$1.4 \times 10^{-1} \pm 0.03$	0.87 ± 0.10

thinning and a decrease in the power-law index, the opposite trend is observed in extension. The observed diameter decay results in an extensional power-law index that increases with increasing xanthan gum concentration, meaning that the higher-concentration solutions are less extensionally thinning than the lower-concentration solutions. Because the extension rate in CaBER-DoS is not controlled, but rather dictated by the fluid properties, measurements of extensional viscosity were only possible at very large extension rates in the range of $10^3 < \dot{\epsilon} < 10^4$. These extension rates are well above the extension rates expected in the wake of the cylinder and much larger than the maximum shear rate accessible with our shear rheometer. As a result, a direct comparison between the shear and extensional rheology cannot be made. However, if one assumes that the power-law behavior holds and the extensional viscosity is extrapolated back to an extension rate of $\dot{\epsilon} = 10^2 s^{-1}$, the result is a Trouton ratio of $\mathrm{Tr} = \eta_E/\eta \approx 150$ for the $c = 0.10$ g/L case and $\mathrm{Tr} \approx 15$ for the $c = 0.50$ g/L case. These large Trouton ratios suggest that the xanthan gum solutions may exhibit some elasticity at the very high extension rates tested here. Similar extensional thinning behavior and Trouton ratios were observed by Martín-Alfonso *et al.* [38], who used flow through a hyperbolic contraction to characterize the extensional viscosity of the xanthan gum solutions at significantly higher concentrations than tested here.

IV. RESULTS

We performed a series of VIV experiments for xanthan gum concentrations in the range of $0 < c < 0.50$ g/L, and over the characteristic Reynolds number range of $23 < \mathrm{Re}_{\mathrm{char}} < 100$ and reduced velocity range of $4 < U^* < 10$, in order to investigate the effect of shear thinning on the VIV response of a 1DOF flexibility-mounted cylinder allowed to oscillate in the CF direction. The experiments at a constant Reynolds number were conducted at a constant flow velocity, and the reduced velocity was changed by changing the stiffness of the system. The change in the Reynolds number for different sets of experiments was achieved by changing the incoming flow velocity. Each time history was recorded for 2 min after steady state was achieved. A period of at least 3 min was given between the end of each test and the beginning of the next. The amplitude and frequency of the cylinder's VIV response for all the solutions tested here are presented in Figs. 3 and 4. In these figures, the dimensionless amplitude of oscillations $A^* = A/D$ and the dimensionless frequency of oscillations $f^* = f/f_n$ are plotted, where A is the amplitude of oscillations, f is its frequency, and f_n is the system's natural frequency in air. It is clear from the plots of Fig. 3 that the addition of xanthan gum has a significant impact on the VIV response of the cylinder. For the lower concentrations, $c = 0.10$ g/L, 0.20 g/L, and 0.35 g/L, VIV is observed. However, for the highest concentration tested, $c = 0.50$ g/L, VIV is completely suppressed over the entire range of the characteristic Reynolds numbers accessible in our flow cell, $\mathrm{Re}_{\mathrm{char}} < 100$. The observed VIV response is in the form of oscillations over a range of reduced velocities (the lock-in range) for which the oscillation frequency stays close to the natural frequency of the system (Fig. 4).

The plots of Fig. 3 show that with increasing concentration, the amplitude and width of the lock-in range decrease. At the low concentration of $c = 0.10$ g/L, the VIV response in Fig. 3(a) follows the VIV response of a 1DOF cylinder placed in Newtonian flow. For a 1DOF cylinder in a Newtonian flow, VIV is observed for Reynolds numbers larger than $\mathrm{Re} \approx 18$ [13]. At a constant

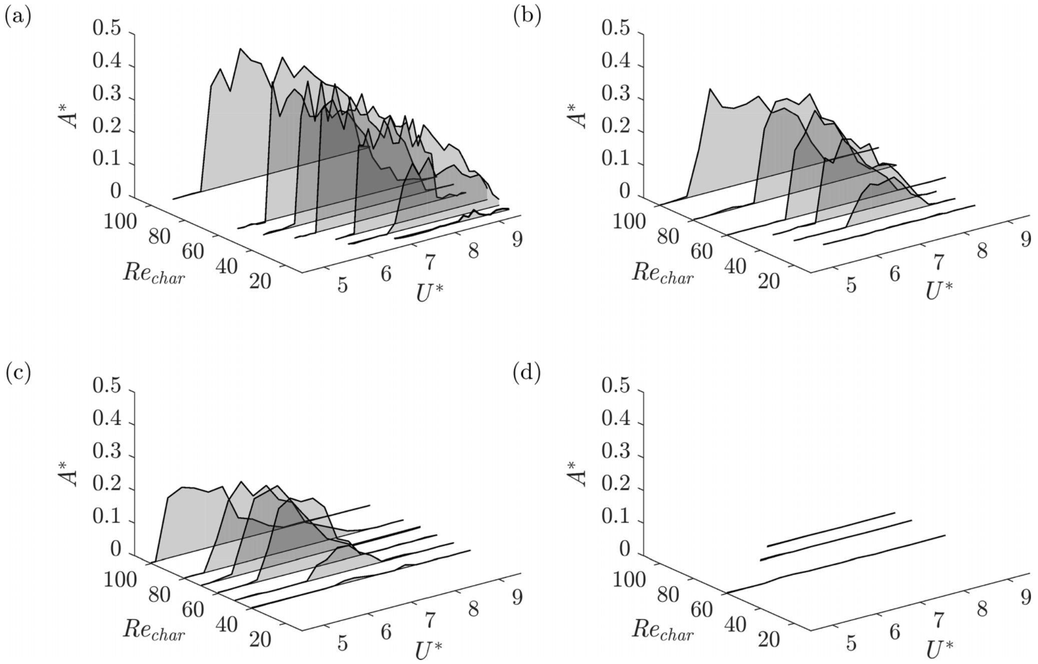

FIG. 3. Amplitude of the VIV response as a function of $\mathrm{Re}_{\mathrm{char}}$ and U^* for various concentrations: (a) 0.10 g/L, (b) 0.20 g/L, (c) 0.35 g/L, and (d) 0.50 g/L. The characteristic shear rates $\dot{\gamma}_{\mathrm{char}}$ range from (a) 9.6 to 45.5 s^{-1}, (b) 24.1 to 64.6 s^{-1}, (c) 42.4 to 86.1 s^{-1}, and (d) 75.0 to 100.0 s^{-1}.

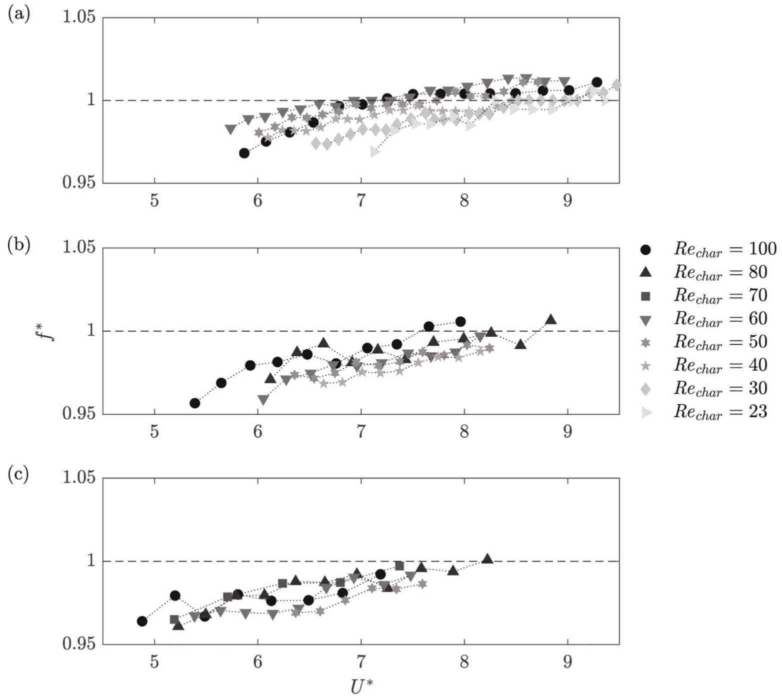

FIG. 4. Normalized frequency in the lock-in range versus U^* for various Reynolds numbers and various concentrations: (a) 0.10 g/L, (b) 0.20 g/L, and (c) 0.35 g/L.

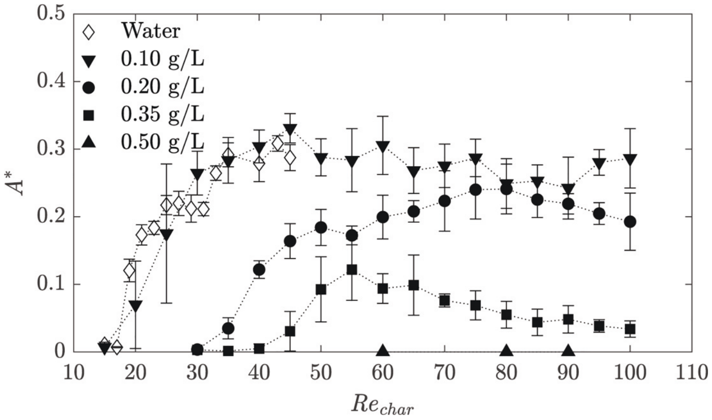

FIG. 5. Amplitude of the VIV response as a function of the Reynolds number at $U^* = 7.5$ for various concentrations. Results for water are from our previous work [13].

reduced velocity, the VIV amplitude for a Newtonian flow increases with Reynolds number from Re = 18 to Re = 33 before reaching a plateau beyond which the amplitude of the VIV response is independent from the Reynolds number [13]. A similar VIV response is observed here for the 0.1 g/L concentration. This is more clearly seen in Fig. 5, where the dimensionless amplitude is plotted as a function of the Reynolds number at a constant reduced velocity of $U^* = 7.5$ for all four concentrations. For comparisons, the VIV response for a Newtonian case (water) based on our previous work [13] is also plotted. The responses for the 0.10 g/L concentration and water very closely match. In both cases, the oscillations begin at $\mathrm{Re}_{\mathrm{char}} = 18$ and the amplitude increases up to $A^* \approx 0.3$ before reaching a plateau. Increasing the xanthan gum concentration increases the critical Reynolds number for the onset of oscillations. For the 0.20 g/L and 0.35 g/L concentrations, VIV is observed at $\mathrm{Re}_{\mathrm{char}} \approx 30$ and $\mathrm{Re}_{\mathrm{char}} \approx 45$, respectively. In all cases, the amplitude of oscillations increases with the Reynolds number before reaching a maximum. This maximum amplitude decreases with increasing concentration until it reaches zero for the 0.50 g/L concentration. For the 0.20 g/L and 0.35 g/L concentrations, the maximum amplitudes at $U^* = 7.5$ are $A^* \approx 0.25$ and $A^* \approx 0.12$, respectively. As the reduced velocities are changed, the mass ratios also change slightly for each case, since we change the reduced velocity by changing the length of the spring that moves with the spring. For the lowest concentration of 0.10 g/L, the mass ratio changes from $m^* = 38$ to $m^* = 46$ for the smallest characteristic Reynolds numbers tested for that concentration (i.e., $\mathrm{Re}_{\mathrm{char}} = 17$) and from $m^* = 26$ to $m^* = 29$ for the largest characteristic Reynolds number (i.e., $\mathrm{Re}_{\mathrm{char}} = 100$). This change decreases as the concentration is increased such that at the highest concentration tested here (i.e., 0.50 g/L), the mass ratio varies from $m^* = 23$ to $m^* = 25$ for all characteristic Reynolds numbers tested at that concentration. We had shown before [13] that such relatively small changes in the mass ratio do not influence the amplitude of observed oscillations.

It is seen in Fig. 5 that the amplitude at $U^* = 7.5$ for the 0.35 g/L concentration does not reach a plateau, but decreases after reaching a maximum around $\mathrm{Re}_{\mathrm{char}} = 55$. This is due to the fact that for the shear thinning fluids studied here, the lock-in range shifts to the left (lower reduced velocities) as the Reynolds number is increased, which in turn results in a shift in the maximum amplitude of oscillations to lower values of reduced velocity (Fig. 3). As a result, if instead of plotting the amplitudes at a constant reduced velocity, we plot the maximum amplitude (Fig. 6), then for the three concentrations that demonstrate VIV, the maximum amplitudes approach a plateau as the Reynolds number is increased. This plateau amplitude decreases from $A^* = 0.41$ to 0.30 to 0.22 and to 0 as the concentration is increased from 0.10 g/L to 0.50 g/L.

The observed shift of the lock-in range to lower reduced velocities and the decrease in the width of the lock-in range with increasing Reynolds numbers are clearly highlighted in the plots of Fig. 7,

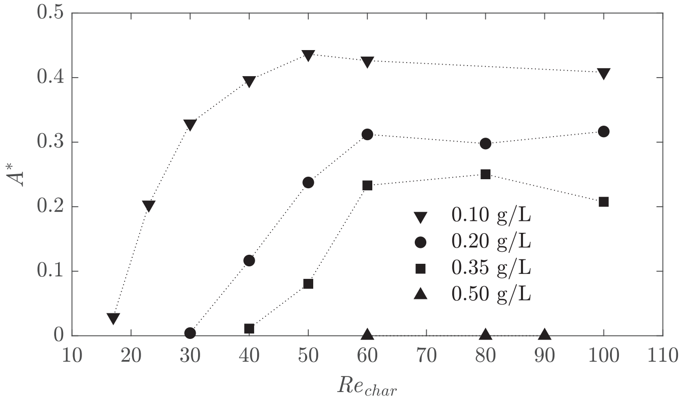

FIG. 6. Maximum amplitude of the VIV response versus the Reynolds number for various concentrations.

where the reduced velocities of the onset and end of the lock-in range as well as the width of the lock-in range are plotted versus the characteristic Reynolds number for the three shear-thinning cases that undergo VIV. From the plot of Fig. 7(a), it is clear that the U^* values at which the lock-in begins and ends decrease as the Reynolds number is increased. Also, at a constant Reynolds number, as the fluid concentration increases, the critical reduced velocities decrease. Therefore, increasing shear-thinning effects and the Reynolds number both result in a shift of the lock-in range to lower U^* values. From the plot of Fig. 7(b), it is clear that at a constant concentration, the lock-in width tends to increase as the Reynolds number is increased until it reaches a plateau at the higher Reynolds numbers. At a constant characteristic Reynolds number, the width of the lock-in range decreases as the concentration is increased.

In all cases where VIV is observed, the dimensionless oscillation frequencies stay close to one, $f^* \approx 1$, as shown in the plots of Fig. 4. These frequency plots also show how the lock-in range

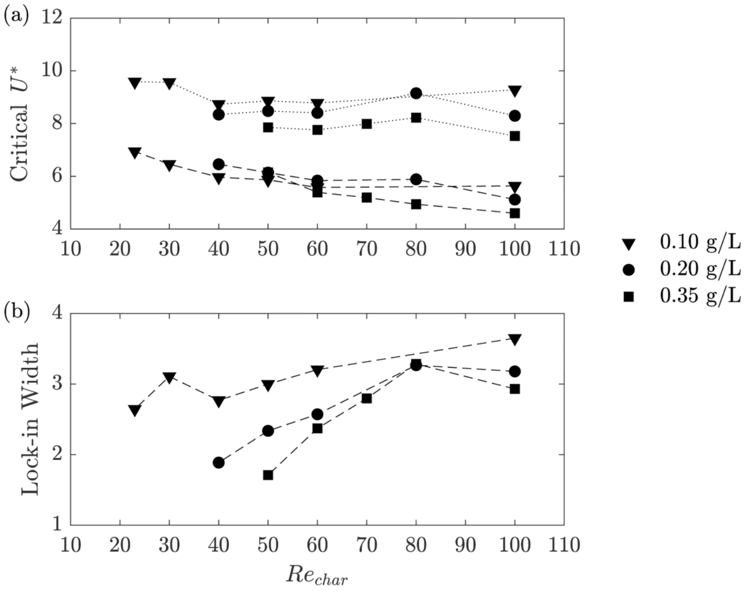

FIG. 7. (a) Critical values of the reduced velocity U^* for the onset (−−−-) and end (.........) of the lock-in range, and (b) the lock-in width as a function of the characteristic Reynolds number.

moves toward smaller reduced velocities as the concentration is increased. Another trend that is observed in the frequency plots is that at each concentration, the frequencies decrease slightly as the Reynolds number is decreased. For example, for the concentration of 0.10 g/L, at the beginning of the lock-in range, the reduced frequency is less than one, $f^* < 1$, for all Reynolds numbers. Then, as the reduced velocity is increased, the frequency ratio reaches one for a range of reduced velocities. Toward the end of the lock-in range, for $\mathrm{Re}_{\mathrm{char}} > 50$, the reduced frequency is greater than one, $f^* > 1$, but does not reach one for smaller Reynolds numbers. This trend is also observed for higher concentrations of 0.20 g/L and 0.35 g/L. For both cases, frequencies increase slightly within the lock-in range, but they cross one only for $\mathrm{Re}_{\mathrm{char}} > 70$. This behavior was observed previously in the numerical results of Patel *et al.* [29] as well. As discussed there, the crossing of one in the frequency plot corresponds to a jump in phase between the displacement and the force from $\phi = 0^\circ$ to $\phi = 180^\circ$, and the appearance of a large contribution of the third harmonic in the force. When the reduced frequency remains smaller than one, $f^* < 1$, the large third harmonic component of the force and the sudden phase shift are not observed in the response, and displacement and force stay in phase.

A major finding of this work is that at a constant characteristic Reynolds number, the amplitude of the VIV response decreases as the xanthan gum concentration (and therefore the degree of shear thinning) is increased. At first glance, this result directly contradicts the conclusion drawn by Patel *et al.* [29]. In their numerical simulations of similar shear-thinning and shear-thickening fluids, they showed that although the degree of shear thinning can affect the extent of the wake, when the results are compared at the same characteristic Reynolds number, as done here, the amplitude and frequency of oscillations are insensitive to the power-law index or the zero-shear-rate viscosity for shear thinning, shear thickening, and Newtonian fluids. The question of why the experiments performed here show such a strong dependence on xanthan gum concentration at a constant characteristic Reynolds number then arises. One possible explanation could be the constitutive model used in the simulations of Patel *et al.* The simulations used a Carreau-Yasuda model to describe the fluid, a model meant for reproducing the power-law dependence of the shear viscosity, which was the goal of that study. However, that model does not distinguish between shear and extensional flows, and as a result, the extensional viscosity of the Carreau-Yasuda model will decay with the same power-law exponent as in shear, and the Trouton ratio at all extension rates will be that of a Newtonian fluid, $Tr = 3$. Conversely, as described in Sec. III, the xanthan gum solutions have an extensionally thinning viscosity that is different from their shear-thinning viscosity. In fact, the extensional power-law exponent increases as fluid concentration increases. This means that as the fluid becomes more shear thinning it becomes less extensional thinning, resulting in Trouton ratios that are much larger than the Newtonian limit, $\mathrm{Tr} > 3$. The flow upstream of the cylinder is in compression, and the flow in the wake of the cylinder is in extension, as is the flow between the shed vortices. As a result, the flow around the cylinder is not pure shear, but has mixed flow kinematics. It is possible, therefore, that the differences in the rheological properties predicted by the constitutive model used in the simulation of Patel *et al.* [29] and the rheological properties measured experimentally for the xanthan gum solutions here are the cause of the differences between the results from simulations and experiments.

To explore the shear and extension rates in the wake of the cylinder in more detail, in Fig. 8 we plot the local extension and shear rates on top of the vortices shed from a fixed cylinder placed in a fluid with 0.20 g/L concentration and at $\mathrm{Re}_{\mathrm{char}} = 80$. The velocity field calculated from PIVLAB is used to calculate the local strain rate tensors. The local extension rate is defined as $\dot{\epsilon} = (\partial u_x/\partial x - \partial u_y/\partial y)/2$, where x is in the direction of flow and y is perpendicular to that; the local shear rate as $\dot{\gamma} = \partial u_x/\partial y + \partial u_y/\partial x$; and the local vorticity as $\vec{\omega} = \nabla \times \vec{u}$, where the velocity vector is $\vec{u} = u_x\hat{i} + u_y\hat{j}$. The vorticity, shear rate, and extension rate in Fig. 8 are then normalized by their respective maximum values. In Fig. 8(a), only the vorticity is shown, and in Figs. 8(b) and 8(c), the local shear rate and extension rate are superimposed over the vorticity to identify regions dominated by shear and extension. Upstream of the cylinder, a region of compression ($\dot{\epsilon} < 0$) is observed, followed by a

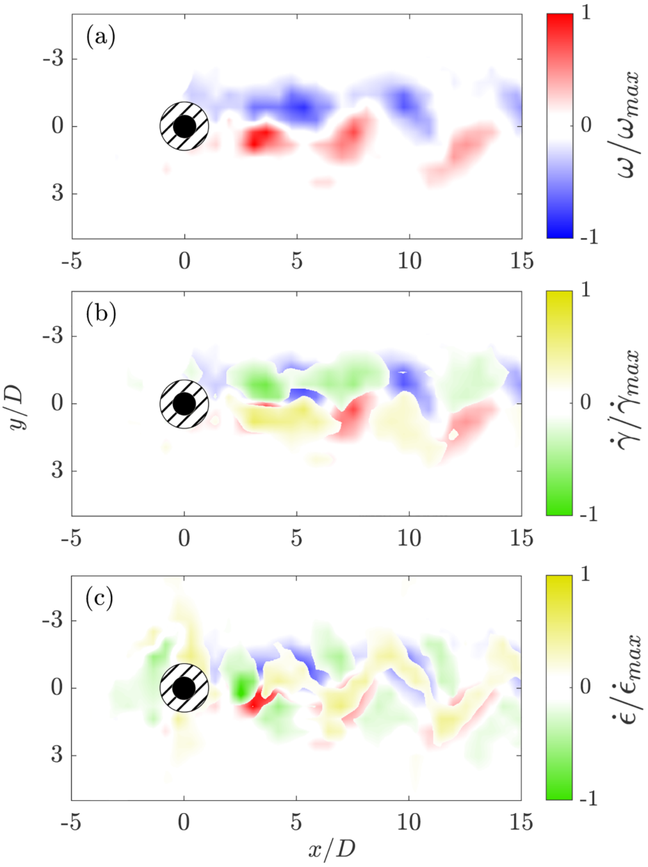

FIG. 8. (a) Normalized vorticity $\omega/\omega_{\mathrm{max}}$, where $\omega_{\mathrm{max}} \approx 34\ \mathrm{s}^{-1}$; (b) normalized shear rate $\dot{\gamma}/\dot{\gamma}_{\mathrm{max}}$, where $\dot{\gamma}_{\mathrm{max}} \approx 45\ \mathrm{s}^{-1}$, overlayed on normalized vorticity; and (c) normalized strain rate $\dot{\epsilon}/\dot{\epsilon}_{\mathrm{max}}$, where $\dot{\epsilon}_{\mathrm{max}} \approx 25\ \mathrm{s}^{-1}$, overlayed on normalized vorticity, plotted in the wake of a fixed cylinder at a concentration of 0.20 g/L and a Reynolds number of $\mathrm{Re}_{\mathrm{char}} = 80$. The hatched area represents the location close to the cylinder where the PIV results are not reliable due to the experimental resolution.

region of strong shear along the cylinder's equator. In the near wake of the cylinder, regions of both high shear and extension rates are observed. In the far wake, also regions of high shear and extension rates are observed between the vortices, while regions of uniaxial extension are observed linking the vortices together and within the vorticies themselves as they are stretched and deformed by the flow. These observations clearly reinforce the need to accurately capture the shear and extensional components of viscosity in future numerical simulations.

The subcritical nature of the observed VIV (i.e., observation of oscillations at Reynolds numbers lower than the critical for the onset of shedding in a rigid cylinder) is exhibited in Fig. 9. In this figure, the wakes of a fixed cylinder (left column) and a flexibly mounted cylinder (right column) are shown at $\mathrm{Re}_{\mathrm{char}} = 50$, with each row representing an increase in the concentration from 0.10 g/L to 0.35 g/L. The flexibly mounted cylinders are at a constant reduced velocity of $U^* = 7.5$. The response for the concentration of 0.10 g/L (first row) is very similar to the Newtonian response. This Reynolds number, $\mathrm{Re}_{\mathrm{char}} = 50$, is very close to the critical Reynolds number of $\mathrm{Re} = 47$ for the onset of shedding in the wake of a fixed cylinder. As a result, weak vortex shedding is observed in the wake of the fixed cylinder in Fig. 9(a). When oscillations are observed, the vortex structure in the wake of the flexibly mounted cylinder becomes more coherent in Fig. 9(b), where

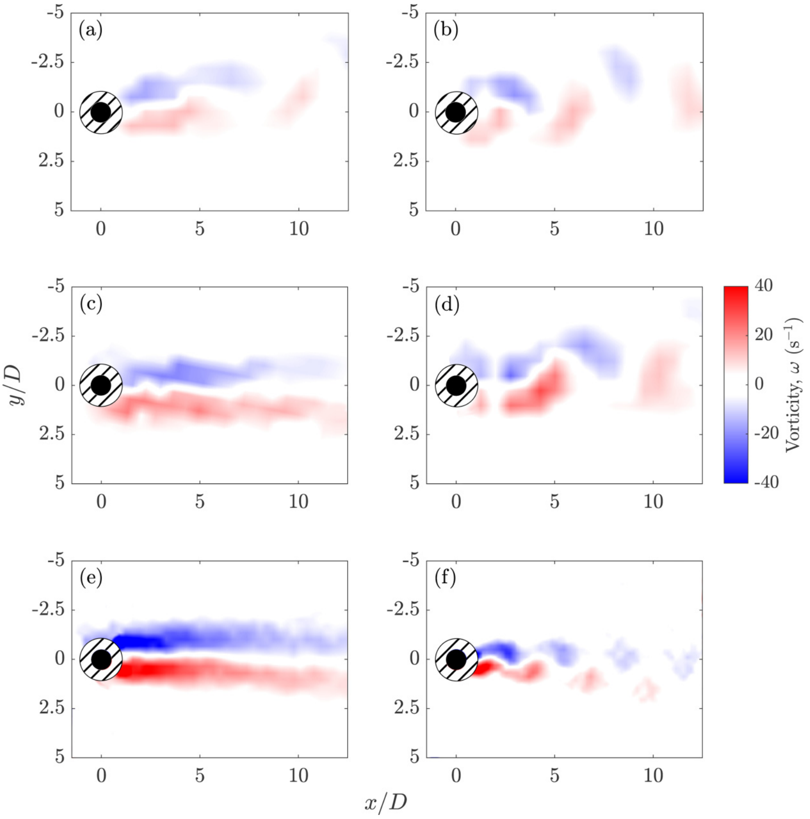

FIG. 9. The wake of a fixed cylinder (left column) and a flexibly- mounting cylinder (right column) at $\mathrm{Re}_{\mathrm{char}} = 50$ and for various concentrations. First row: 0.10 g/L, second row: 0.20 g/L, and third row: 0.35 g/L. The reduced velocity for the flexibly mounted cylinder is $U^* = 7.5$. The hatched area represents the location close to the cylinder where the PIV results are not reliable due to the experimental resolution.

the shedding is enhanced by the cylinder oscillations. When the fluid concentration is increased to 0.20 g/L, the shear layers around the stationary cylinder do not interact, as shown in Fig. 9(c). As a result, the increased shear thinning for concentrations of 0.20 g/L and above suppresses the vortex shedding in the wake of the fixed cylinder at this Reynolds number, $\mathrm{Re}_{\mathrm{char}} = 50$. When the cylinder is flexibly mounted and undergoes VIV, as shown in Fig. 9(d), however, vortex shedding is observed in the wake of the cylinder, highlighting the subcritical nature of this FSI instability. For the 0.20 g/L concentration, the strength of the shed vortices, measured by their vorticity, is larger than the strength of vortices in the wake of the oscillating cylinder in the 0.10 g/L concentration. A similar trend is observed for the 0.35 g/L concentration, where shedding is not observed in the wake of the fixed cylinder [Fig. 9(e)], but observed in the wake of the oscillating cylinder [Fig. 9(f)]. The vorticity increases even further for the 0.35 g/L case. This observation agrees with previous literature which showed that increasing the amount of shear thinning of a fluid will intensify the vorticity close to a fixed cylinder [28,29]. Despite the increasing vorticity, the oscillation amplitude decreases with increasing concentration (Fig. 5). This might appear counterintuitive. However, it can be explained by considering the change in size and location of the shed vortices as the concentration is increased. By considering the vortices in Fig. 9 one notes that with increasing concentration, the vortices become smaller and are shed closer to the wake centerline, resulting in a narrower wake. As a result, the orientation of the fluctuating force that the shed vortices impart on the cylinder shifts from the cross-flow direction more toward the inline direction. This shift in the orientation

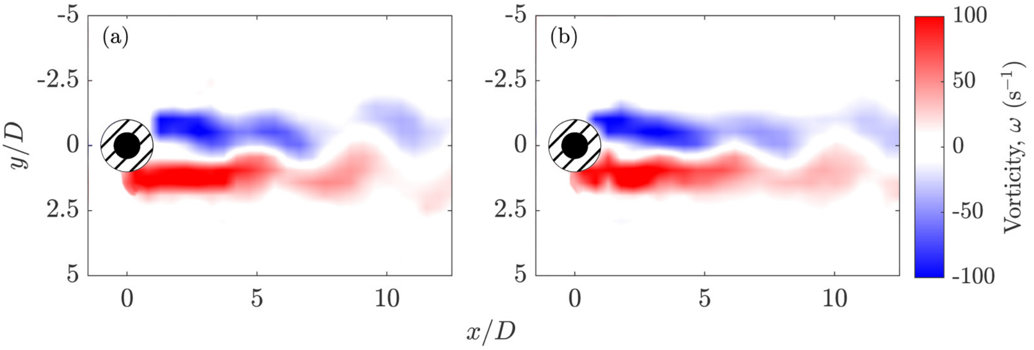

FIG. 10. The wake of (a) a fixed cylinder and (b) a flexibly mounting cylinder at $\mathrm{Re}_{\mathrm{char}} = 90$ and a concentration of 0.50 g/L. The reduced velocity for the flexibly mounted cylinder is $U^* = 7.5$. The hatched area represents the location close to the cylinder where the PIV results are not reliable due to the experimental resolution.

reduces the magnitude of the fluctuating force in the y direction and could contribute to the observed decrease in the oscillation amplitude with increasing concentration.

At the highest concentration tested, 0.50 g/L, no oscillations are observed for the Reynolds numbers tested here ($\mathrm{Re}_{\mathrm{char}} \leqslant 90$), including $\mathrm{Re}_{\mathrm{char}} = 50$. The wakes of a fixed and a flexibly mounted cylinder for this concentration are shown in Fig. 10 at $\mathrm{Re}_{\mathrm{char}} = 90$. Since no oscillations are observed, no significant difference is observed between the wakes in the plots. Clearly vortices are shed in the wake as expected for a cylinder placed in the flow at this Reynolds number. The vortices are shed roughly at a distance $x/D = 10$ downstream of the cylinder, which is much farther downstream than where the vortices are shed for the cases of lower concentration. As a result, the fluctuating forces that these vortices exert on the cylinder are not large enough to induce measurable cylinder motion. For the 0.50 g/L concentration, VIV might be observed at larger Reynolds numbers, i.e., $\mathrm{Re}_{\mathrm{char}} > 90$, which were not tested here as our experimental setup was limited to a maximum Reynolds number of $\mathrm{Re}_{\mathrm{max}} = 90$ for the 0.50 g/L concentration. We should note that a decrease in the vortex formation length with increasing Reynolds number was observed in the 0.20 g/L case for both the fixed and the oscillating cylinder. Similar changes to the formation length were also observed numerically for a cylinder in the cross flow of a power-law fluid [21,29]. Therefore, we expect that as the Reynolds number is increased past $\mathrm{Re}_{\mathrm{char}} = 90$ in the case of 0.50 g/L concentration, the formation length of the shed vortices will decrease and eventually the vortices will shed close enough to the cylinder to induce oscillations, but at a Reynolds number much larger than that of either a Newtonian or a weakly shear-thinning fluid.

V. CONCLUSIONS

It is well known that a flexibly mounted rigid cylinder placed in a Newtonian fluid undergoes VIV at Reynolds numbers above $\mathrm{Re} = 18$. In this paper, we experimentally investigate the role of fluid rheology on VIV by replacing the Newtonian fluid with a series of shear-thinning xanthan gum solutions in water. We increase the concentration in a range from 0.10 g/L to 0.50 g/L, and by increasing the concentration, we increase the strength of the shear-thinning effects. This manifests itself as a decrease in the power-law index from $n = 0.9$ to $n = 0.6$ with increasing concentration. We show that when the fluid is made shear thinning, the response of the flexibly mounted cylinder differs from the Newtonian response in several ways. First, at a constant Reynolds number, the amplitude of the cylinder oscillations decreases with increasing xanthan gum concentration. For example, with increasing concentration at $\mathrm{Re}_{\mathrm{char}} = 60$, the dimensionless oscillation amplitude decreases from $A^* = 0.42$ to 0.30 to 0.23 and to 0.0 as the concentration is increased from $c = 0.10$

to 0.20 to 0.35 and to 0.50 g/L. Second, with increasing xanthan gum concentration, the lock-in range is shifted to lower reduced velocities and the width of the lock-in range is reduced. For example, at $\mathrm{Re}_{\mathrm{char}} = 60$, the width of the lock-in range is reduced from $\Delta U^* = 3.1$ to 2.2 as the concentration is increased from 0.10 to 0.35 g/L. The critical characteristic Reynolds number at which oscillations are first observed increases with increasing xanthan gum concentration. In fact, at the highest concentration studied here, VIV is completely suppressed at the Reynolds number accessible in our experimental setup. The critical Reynolds number to observe VIV increases from $\mathrm{Re}_{\mathrm{crit}} = 18$ (which is also the critical Reynolds number for VIV in Newtonian fluids) to 30 to 40 and to $\mathrm{Re}_{\mathrm{crit}} > 90$ as the concentration of xanthan gum is increased from $c = 0.10$ to 0.20 to 0.35 and to 0.50 g/L.

ACKNOWLEDGMENT

This work was funded by the National Science Foundation under Grant No. CBET-2126175.

[1] T. Sarpkaya, A critical review of the intrinsic nature of vortex-induced vibrations, J. Fluids Struct. **19**, 389 (2004).

[2] C. Williamson and R. Govardhan, Vortex-induced vibrations, Annu. Rev. Fluid Mech. **36**, 413 (2004).

[3] M. P. Païdoussis, S. J. Price, and E. D. Langre, *Fluid-Structure Interactions: Cross-Flow-Induced Instabilities*, 2nd ed. (Cambridge University Press, Cambridge, 2014).

[4] Y. Modarres-Sadeghi, *Introduction to Fluid-Structure Interactions* (Springer Nature, Cham, 2021).

[5] N. Cagney and S. Balabani, Fluid forces acting on a cylinder undergoing streamwise vortex-induced vibrations, J. Fluids Struct. **62**, 147 (2016).

[6] T. D. Gurian, T. Currier, and Y. Modarres-Sadeghi, Flow force measurements and the wake transition in purely inline vortex-induced vibration of a circular cylinder, Phys. Rev. Fluids **4**, 034701 (2019).

[7] B. M. Benner and Y. Modarres-Sadeghi, Vortex-induced vibrations of a one-degree-of-freedom cylinder transitioning from the inline to the crossflow degree of freedom, Phys. Rev. Fluids **6**, 114702 (2021).

[8] J. M. Dahl, F. S. Hover, M. S. Triantafyllou, S. Dong, and G. E. Karniadakis, Resonant Vibrations of Bluff Bodies Cause Multivortex Shedding and High Frequency Forces, Phys. Rev. Lett. **99**, 144503 (2007).

[9] J. Dahl, F. Hover, M. Triantafyllou, and O. Oakley, Dual resonance in vortex-induced vibrations at subcritical and supercritical Reynolds numbers, J. Fluid Mech. **643**, 395 (2010).

[10] D. W. Carlson, T. M. Currier, and Y. Modarres-Sadeghi, Flow-induced vibrations of a square prism free to oscillate in the cross-flow and inline directions, J. Fluid Mech. **919**, A2 (2021).

[11] C. Mathis, M. Provansal, and L. Boyer, The Benard-Von Karman instability: An experimental study near the threshold, J. Phyique Lett. **45**, 483 (1984).

[12] S. Mittal and S. Singh, Vortex-induced vibrations at subcritical Re, J. Fluid Mech. **534**, 185 (2005).

[13] P. R. Boersma, J. Zhao, J. P. Rothstein, and Y. Modarres-Sadeghi, Experimental evidence of vortex-induced vibrations at subcritical Reynolds numbers, J. Fluid Mech. **922**, R3 (2021).

[14] R. Bourguet, Vortex-induced vibrations of a flexible cylinder at subcritical Reynolds number, J. Fluid Mech. **902**, R3 (2020).

[15] A. Dey, Y. Modarres-Sadeghi, and J. Rothstein, Experimental observation of viscoelastic fluid-structure interactions, J. Fluid Mech. **813**, R5 (2017).

[16] A. A. Dey, Y. Modarres-Sadeghi, and J. P. Rothstein, Viscoelastic fluid-structure interactions between a flexible cylinder and wormlike micelle solution, Phys. Rev. Fluids **3**, 063301 (2018).

[17] A. Dey, A. Lindner, Y. Modarres-Sadeghi, and J. Rothstein, Oscillations of a cantilevered micro beam driven by a viscoelastic flow instability, Soft Matter **16**, 1227 (2020).

[18] A. Dey, Y. Modarres-Sadeghi, and J. Rothstein, Viscoelastic flow-induced oscillations of a cantilevered beam in the crossflow of a wormlike micelle solution, J. Non-Newtonian Fluid Mech. **286**, 104433 (2020).

[19] C. Hopkins, S. Haward, and A. Shen, Purely elastic fluid–structure interactions in microfluidics: Implications for mucociliary flows, Small **16**, 1903872 (2020).

[20] A. Dey, Y. Modarres-Sadeghi, and J. Rothstein, Observation of lock-in for viscoelastic fluid-structure interactions, J. Fluids Struct. **96**, 103025 (2020).

[21] P. M. Coelho and F. T. Pinho, Vortex shedding in cylinder flow of shear-thinning fluids. I. Identification and demarcation of flow regimes, J. Non-Newtonian Fluid Mech. **110**, 143 (2003).

[22] D. Richter, G. Iaccarino, and E. S. G. Shaqfeh, Effects of viscoelasticity in the high Reynolds number cylinder wake, J. Fluid Mech. **693**, 297 (2012).

[23] P. M. Coelho and F. T. Pinho, Vortex shedding in cylinder flow of shear-thinning fluids. II. Flow characteristics, J. Non-Newtonian Fluid Mech. **110**, 177 (2003).

[24] P. M. Coelho and F. T. Pinho, Vortex shedding in cylinder flow of shear-thinning fluids. III. Pressure measurements, J. Non-Newtonian Fluid Mech. **121**, 55 (2004).

[25] S. Bailoor, J. Seo, and R. Mittal, Vortex shedding from a circular cylinder in shear-thinning Carreau fluids, Phys. Fluids **31**, 011703 (2019).

[26] M. Alam, A. Raj, P. M. Khan, S. Kumar, and S. Roy, Numerical simulation of flow of a shear-thinning Carreau fluid over a transversely oscillating cylinder, J. Fluid Mech. **921**, A23 (2021).

[27] Ç. Şahin and K. Atalık, Comparison of inelastic and elastic non-Newtonian effects on the flow around a circular cylinder in periodic vortex shedding, J. Non-Newtonian Fluid Mech. **263**, 1 (2019).

[28] I. Lashgari, J. O. Pralits, G. Flavio, and B. Luca, First instability of the flow of shear-thinning and shear-thickening fluids past a circular cylinder, J. Fluid Mech. **701**, 201 (2012).

[29] U. N. Patel, J. P. Rothstein, and Y. Modarres-Sadeghi, Vortex-induced vibration of a cylinder in inelastic shear-thinning and shear-thickening fluids, J. Fluid Mech. **934**, A39 (2022).

[30] W. Thielicke and R. Sonntag, Particle image velocimetry for MATLAB: Accuracy and enhanced algorithms in PIVlab, J. Open Res. Software **9**, 12 (2021).

[31] F. A. Morrison, *Understanding Rheology* (Oxford University Press, New York, 2001).

[32] J. Dinic, Y. Zhang, L. N. Jimenez, and V. Sharma, Extensional relaxation times of dilute, aqueous polymer solutions, ACS Macro Lett. **4**, 804 (2015).

[33] J. Dinic, L. N. Jimenez, and V. Sharma, Pinch-off dynamics and dripping-onto-substrate (DoS) rheometry of complex fluids, Lab Chip **17**, 460 (2017).

[34] S. Sur and J. P. Rothstein, Drop breakup dynamics of dilute polymer solutions: Effect of molecula weight, concentration, and viscosity, J. Rheology **62**, 1245 (2018).

[35] M. Rosello, S. Sur, B. Barbet, and J. P. Rothstein, Dripping-onto-substrate capillary breakup extensional rheometry of low-viscosity printing inks, J. Non-Newtonian Fluid Mech. **266**, 160 (2019).

[36] G. H. McKinley, Visco-elasto-capillary thinning and break-up of complex fluids, The British Society of Rheology 1 (2005), https://dspace.mit.edu/handle/1721.1/18085.

[37] P. Doshi, R. Suryo, O. E. Yildirim, G. H. Mckinley, and O. A. Basaran, Scaling in pinch-off of generalized Newtonian fluids, J. Non-Newtonian Fluid Mech. **113**, 1 (2003).

[38] J. E. Martín-Alfonso, A. A. Cuadri, M. Berta, and M. Stading, Relation between concentration and shear-extensional rheology properties of xanthan and guar gum solutions, Carbohydr. Polym. **181**, 63 (2018).